

# **A First-principles Study of Weyl Nodal Loop and Multiple Sets of Weyl Points in Trigonal PtBi<sub>2</sub>**

Lin-Lin Wang<sup>1,2\*</sup>

<sup>1</sup>Ames National Laboratory, Ames, IA 50011, USA

<sup>2</sup>Department of Physics and Astronomy, Iowa State University, Ames, IA 50011, USA

[llw@ameslab.gov](mailto:llw@ameslab.gov)

## Abstract

Coexistence of surface superconductivity and Fermi arcs in trigonal  $\gamma$ -PtBi<sub>2</sub> has recently attracted attention for possible realization of topological superconductivity. The Fermi arcs on the two different (0001) surface terminations have been associated with the set of Weyl points just above the Fermi energy ( $E_F$ ). Here using first-principles calculations to explore the band crossings over the full Brillouin zone between the nominally highest valence and lowest conduction bands in  $\gamma$ -PtBi<sub>2</sub>, we find a Weyl nodal loop (WNL) and multiple sets of Weyl points (WPs). The main difference between the two reported experimental structural parameters is the magnitude of Bi-layer buckling. While the WNL, bulk gap region and the set of Weyl points just above the  $E_F$  are robust, the number and location of the other sets of WPs depend sensitively on the structural parameters with different magnitude of Bi-layer buckling. Besides calculating the 2D Fermi surface with Fermi arcs and quasi-particle interference (QPI) around the  $E_F$  in good agreements with ARPES and experimental QPI, we also predict new Fermi arc features at higher energy.

## I. Introduction

Trigonal  $\gamma$ -PtBi<sub>2</sub><sup>1</sup> has shown large linear magnetoresistance<sup>2-4</sup> and its electronic band structure has been studied in earlier works for triply degenerated point<sup>3</sup>, large Rashba-like spin splitting<sup>5</sup> and other interesting surface states<sup>6-8</sup>. More recently the coexistence of surface superconductivity (SC) and Fermi arcs (FAs) on trigonal  $\gamma$ -PtBi<sub>2</sub> (0001) surface has attracted much attention for possible realization of topological superconductivity<sup>9-23</sup>. Surface SC of  $\gamma$ -PtBi<sub>2</sub> has manifested in the SC gap opening<sup>9, 11, 20-22</sup> in scanning tunneling spectroscopy (STS) and contact SC<sup>14, 23</sup> with STS tips, as well as the sharpening of FAs<sup>10, 18</sup> in angle-resolved photo-emission spectroscopy (ARPES). A sizable SC gap opening of a few meV has been reported in a range from 2 K<sup>11, 20, 22</sup> to as high as 45 K<sup>21</sup>. A very recent low-temperature STS study<sup>20</sup> has discovered the SC vortex under magnetic field with high mobility to prove the 2D surface SC in  $\gamma$ -PtBi<sub>2</sub>. The pairing mechanism and possible Majorana particles are still being actively investigated<sup>19, 24, 25</sup>. The FAs on the two different (0001) surface terminations have been associated with the set of inversion-breaking Weyl points (WPs) just above the Fermi energy ( $E_F$ )<sup>10, 16</sup>.

Here using density functional theory<sup>26, 27</sup> (DFT) calculations and Wannier functions<sup>28-30</sup>, we explore the band crossings throughout the full Brillouin zone (BZ) between the nominally highest valence and lowest conduction bands in  $\gamma$ -PtBi<sub>2</sub> with different experimental and averaged structural parameters. We find a Weyl nodal loop (WNL) and multiple sets of Weyl points (WPs), and the number of the WP sets depends on the small changes in structural parameters. The main difference between the two experimentally reported structural parameters<sup>1, 12</sup> is the magnitude of the Bi-layer buckling. In contrast to the robustness of WNL on the  $\Gamma$ - $K$ - $A$  plane, the bulk gap region and the Set 1 WPs along the  $\bar{\Gamma}$ - $\bar{M}$  direction, we find the number and locations of the other sets of WPs are sensitive to the Bi-layer buckling by using both the more and less Bi-layer buckling structures as well as the averaged one. We also study the evolution of the FAs and surface states around the bulk gap region. Besides calculating the 2D Fermi surface (FS) with FAs and quasi-particle interference (QPI) in good agreements with ARPES<sup>10, 16</sup> and experimental QPI<sup>17, 20</sup>, we also predict additional FAs on the other side of WP projection at higher energy above the  $E_F$ . Our detailed mapping of the WNL, multiple sets of WPs, FAs and QPI in  $\gamma$ -PtBi<sub>2</sub> provides a better understanding of experimental observations.

## II. Computational Methods

Band structures of  $\gamma$ -PtBi<sub>2</sub> in space group 157 with spin-orbit coupling (SOC) have been calculated in DFT with PBE<sup>31</sup> exchange-correlation (XC) functional and modified Becke-Johnson (mBJ)<sup>32</sup> exchange potential, a plane-wave basis set and projected augmented wave method<sup>33</sup> as implemented in VASP<sup>34, 35</sup>. A Monkhorst-Pack<sup>36</sup> (8×8×8)  $k$ -point mesh with a Gaussian smearing of 0.05 eV including the  $\Gamma$  point and a kinetic energy cutoff of 230.3 eV have been used. Besides the two experimental<sup>1, 12</sup> and averaged structural parameters for band structure calculations, the atomic positions have also been relaxed in PBE<sup>31</sup> and XC functionals with van der Waals (vdW) interactions including D3<sup>37</sup>, optB86b<sup>38</sup>, r2SCAN+rVV10<sup>39</sup> with lattice constants fixed to experimental values<sup>1</sup> to compare the relaxed internal structural parameters to experiment. The atomic positions are relaxed with the remaining absolute force on each atom being less than 0.02 eV/Å. To explore the band structure and surface states, tight-binding models based on maximally localized Wannier functions<sup>28-30</sup> have been constructed to reproduce closely the bulk band structure including SOC in the range of  $E_F \pm 2$  eV with Pt *sd* and Bi *p* orbitals. The surface spectral function, 2D Fermi surface with Fermi arcs of the semi-infinite surface and QPI as joint density of states<sup>40</sup> have been calculated with the surface Green's function methods<sup>41, 42</sup> as implemented in WannierTools<sup>43</sup>.

## III. Results and Discussion

Figure 1 presents the bulk crystal and band structures of trigonal  $\gamma$ -PtBi<sub>2</sub>. The crystal structure of  $\gamma$ -PtBi<sub>2</sub> in space group P31m (157) is shown in Fig.1(a), which has no inversion symmetry, but a set of vertical mirror planes combined with the 3-fold rotation symmetry. The structure is formed with stacking Bi-Pt-Bi layers along the *c*-axis, which has three different types of Bi sites, giving two different terminations on (0001) surface. The A-termination has a buckled Bi layer with Bi1 and Bi2 sites, while the B-termination has a flat Bi layer with Bi3 site. These two different terminations have shown different SC behavior and surface band structures. For the structural parameters of  $\gamma$ -PtBi<sub>2</sub>, there are two experimental reports, one in 2014<sup>1</sup> and the other in 2020<sup>12</sup>, which has a major difference in the magnitude of the buckling of the Bi layer in the A-termination. As listed in Table 1, between the two sets of experimental structural parameters for  $\gamma$ -PtBi<sub>2</sub>, the

lattice constants of  $a$  and  $c$  are almost the same, which are also plotted in Fig.2 for the deviation with respect to the 2014 experimental values<sup>1</sup>. The internal coordinates of Pt and Bi3 sites, i.e.,  $x_{\text{Pt}}$ ,  $x_{\text{Bi3}}$  and  $z_{\text{Bi3}}$  are also similar between the two experiments as shown by the red bars in Fig.2. However, there is a sizable difference for the  $z$  values of Bi2 and Bi1 sites as their in-plane positions are at the ideal (0, 0) and (1/3, 2/3). The 0.292 of  $z_{\text{Bi2}}$  in Ref. <sup>12</sup> is larger than the 0.28429 in Ref. <sup>1</sup>, while the 0.127 of  $z_{\text{Bi1}}$  is smaller than the 0.15486, which results in a larger Bi layer buckling,  $d_{\text{Bi2-Bi1}}$ , of 0.955 Å in Ref. <sup>12</sup> than 0.798 Å in Ref. <sup>1</sup> for the vertical interlayer distance between Bi2 and Bi1. Such a difference of 0.157 Å as plotted in Fig.2 seems small at first glance, but we will show later that they result in different sets of WPs as well as FA connectivity.

To validate the difference in the experimental structural parameters, we have used four different types of XC functionals in DFT to relax the internal atomic positions by fixing the unit cell lattice constants to Ref.<sup>1</sup>, because the difference in the two experimental lattice constants is very small. The four XC functionals include PBE and three with explicit vdW interactions, namely, D3 with empirical vdW interaction<sup>37</sup>, optB86b with nonlocal vdW functional<sup>38</sup> and the latest r2SCAN+rVV10<sup>39</sup>. Among the four relaxed structures as listed in Table 1 and plotted in Fig.2, again, the deviations of Pt and Bi3 are small, and their values are close to those reported in both experiments. For  $z_{\text{Bi2}}$ , the four relaxed values are all smaller than Ref.<sup>1</sup>. For  $z_{\text{Bi1}}$ , the relaxed values are in between the two experimental values and closer to Ref.<sup>1</sup>, except for r2SCAN+rVV10, which is slightly larger than Ref.<sup>1</sup>. As for the buckling of  $d_{\text{Bi2-Bi1}}$ , the relaxed values are slightly larger except for r2SCAN+rVV10 with a slightly smaller value than Ref.<sup>1</sup>. Overall, as compared and plotted in Fig.2, the DFT-relaxed atomic positions are closer to those of Ref.<sup>1</sup> than Ref.<sup>12</sup>. Usually using experimental lattice constants to correct the over/underestimation of DFT with relaxed atomic positions are good choices for band structure calculations. Here the two reported lattice constants are almost the same, while the largest difference is in  $z_{\text{Bi2}}$  and  $z_{\text{Bi1}}$ , i.e., with more or less Bi-layer buckling in  $d_{\text{Bi2-Bi1}}$ . Thus, we will also use the averaged structural parameters between these two experimental reports as listed in Table 1 and plotted in Fig.2 (blue bar) to study the changes in band structure induced by the different magnitude of the Bi-layer buckling.

The projected density of states (PDOS) in Fig.1(b) shows that the band hybridization and chemical bonding are mostly between the Pt 5d and Bi 6p orbitals. Around the  $E_F$ , there is a local minimum of DOS. When inspecting the band structure in Fig.1(d), along the  $\Gamma$ - $M$ - $K$ - $\Gamma$  direction on the  $k_z=0.0$  plane, it is semi-metallic with a major band inversion along the  $\Gamma$ - $M$  direction. But going to the  $k_z=0.5$  plane, the band structure is more metallic with large dispersive band crossing  $E_F$ . There are totally five bands crossing the  $E_F$  and the 3D Fermi surface is plotted in Fig.1(c). The major FS sheets are near the  $k_z=0.5$ , while near the  $k_z=0.0$  plane, there are pairs of small electron and hole pockets, echoing the band structure plot in Fig.1(d). The touching pockets near  $k_z=0.0$  plane gives the robust Set 1 WPs from the main band inversion along the  $\Gamma$ - $M$  direction, while the large pockets near  $k_z=0.5$  gives the WNL and most of the other sets of WPs. For the WNL, as zoomed in Fig.1(f) along the  $H$ - $A$  direction, there are two crossing points, one at  $E_F$  and the other near  $E_F-0.80$  eV, showing the large range of dispersion for these bands. By fitting to a tight-binding model with Wannier functions to reproduce the band structure closely within  $E_F\pm2.00$  eV, we can efficiently search over the full BZ to map out the WNL as plotted in Fig.1(g) with the contours of zero band gap on the  $k_y$ - $k_z$  plane, because the loop is protected by the  $M_x$  mirror symmetry. We also find six sets of WPs, which are plotted in Fig.1(e) together with the WNL, and their momentum-energy are listed in Table 2. Each listed WP can be used to produce the other 11 WPs in the same set because they are related by time-reversal, rotation and mirror symmetries with the corresponding chirality. To better show WP positions, we have projected them on the  $k_x$ - $k_y$  or (0001) plane in the surface BZ as shown in Fig.1(h). Among them, Set 1 WPs are halfway along the  $\bar{\Gamma}$ - $\bar{M}$  direction as labeled, while the other five sets are near the  $\bar{\Gamma}$ - $\bar{K}$  direction and close to the WNL. The band dispersion of WP set 1 and 2 are plotted in Fig.1(i) as they are near the  $E_F$ . Fig.(j-k) show the other four sets of WPs, which are further above the  $E_F$ .

When the input structural parameters are switched to Ref.<sup>12</sup> with more Bi-buckling, the number of WP set is reduced to two as listed in Table 2. Set 1 WPs remain just above the  $E_F$  at 0.033 eV and still close to the  $\Gamma$ - $M$  direction. In contrast, when switching to Ref.<sup>1</sup> with less Bi-buckling, the number of WP sets becomes five as listed in Table 2. Besides Set 1 WPs being moved to 0.072 eV. Set 2 WPs are moved to just below the  $E_F$  at -0.015 eV and become also close to the  $\Gamma$ - $M$  direction and  $k_z=0.0$  plane. With all the three

structural parameters, the WNL is persistent as it is protected by the mirror symmetry and Set 1 WPs are also robust as it is from the main band inversion along the  $\Gamma$ - $M$  direction. The extra set of WPs about 0.16 eV above the  $E_F$  has been noticed before with the more Bi-buckling structure. But here we find it is remarkable that the two different experimental structural parameters give quite different number of extra WP sets, although the difference in Bi-layer buckling is only 0.157 Å. Importantly from this structural variation, we demonstrate that Set 1 WPs just above the  $E_F$  and close to the  $\Gamma$ - $M$  direction are very robust. While the extra sets of WPs at higher energy and close to the  $\Gamma$ - $K$  direction are more susceptible to the change in structural parameters. In a way, the WNL acts as a generator of extra sets of WPs with additional band inversion just off the  $\Gamma$ - $K$  direction. In the remaining of the paper, we will present and compare the surface band structures from these three different structural parameters. We will also compare their FAs and the associated QPI to both ARPES and experimental QPI spectra, and we find the results from the averaged structural parameters give the best match to these experiments so far.

Figures 3 and 4 compare the 2D FS and QPI of  $\gamma$ -PtBi<sub>2</sub> (0001) calculated with the three different structural parameters around the  $E_F$  at -0.012 eV and +0.012 eV, respectively. The 2D FS from Fig.3 and 4 are also zoomed in Fig.5 around Set 1 WPs. First midway along the  $\bar{\Gamma}$ - $\bar{M}$  direction, all the three cases have the projected bulk gap region, which is the signature from the main band inversion along the  $\Gamma$ - $M$  and  $A$ - $L$  directions as seen in Fig.1(d). For the 2D FS at -0.012 eV in Fig.3(a) with the averaged structure, the FAs compare well with ARPES (Fig.3(a) of Ref.<sup>16</sup>) showing a waterdrop shape, and the merge into the projection of Set 1 WPs is better seen in Fig.4(a) at +0.012 eV with zoomed in Fig.5(a) and Fig.5(c). The similar shape of the FAs is also seen from the calculation with the more Bi-buckling structure in Fig.3(e) with zoomed in Fig.5(e). The corresponding QPI in Fig.3(f) also agrees with the previous calculation (Fig.3(C) of Ref.<sup>17</sup>). We notice that with the same more Bi-buckling structure<sup>12</sup>, we can only get the two sets of WPs and the associated FAs using mBJ, but not the regular PBE XC functional as specified in Ref.<sup>15</sup>. For the QPI from the averaged structure in Fig.3(b), the agreement to experimental QPI (Fig.3(A) of Ref.<sup>17</sup>) is better than Fig.3(b), especially for the three-leaf shape around the  $\bar{K}$  point and the petal shape with high intensity midway along the  $\bar{\Gamma}$ - $\bar{M}$  direction. In contrast, the 2D FS from the less Bi-buckling structure in Fig.3(i) has two sets of WP projections

along the  $\bar{\Gamma}$ - $\bar{M}$  direction, which give a different shape of FAs, smaller and connecting on the other side of Set 2 WP as zoomed in Fig.5(i). They produce a QPI pattern in Fig.5(j) different from previous experimental QPI<sup>17</sup>, but is more in line with the recent experimental QPI (Fig.4(a) of Ref.<sup>20</sup>) with more intensity appearing midway between  $\bar{M}$  and  $\bar{K}$  points. It is possible to observe different QPI patterns from different samples, because there are two different reported structural parameters with different Bi-buckling, whose magnitude can also be affected by strain. Moving to the B-termination in the bottom half of Fig.3, all three structures show similar FAs around the far side of the bulk gap region, although for the less Bi-buckling structure, this FA is spanned by Set 2 WPs just below the  $E_F$  as also zoomed in Fig.5(j). The simulated QPI patterns for the B-termination in the last row of Fig.3 for the three structures agree with each other overall and also the previous experimental QPI (Fig.3(D) of Ref.<sup>17</sup>).

In Fig.4 at +0.012 eV, while the FAs for the averaged structure in Fig.4(a) and more Bi-buckling structure in Fig.4(e) are merged to the rim of the bulk gap region as zoomed in Fig.5.(c) and (g), respectively, the less Bi-buckling structure in Fig.4(i) has the FAs switch toward Set 1 WPs projection with the far side half of the ring breaking off due to Set 2 WPs as zoomed in Fig.5(k). Its calculated QPI in Fig.4(j) now overall resembles the other two structures in Fig.4(b) and (f), but with some local features like the star pattern at the  $\bar{K}$  point. On the B-termination, the FAs from the far side of bulk gap region in Fig.4(c) and (g) show reduced intensity, except for the less Bi-buckling in Fig.4(k), whose FAs intensity is higher as they are spanned by Set 2 WPs with zoomed in Fig.5(l). Interestingly for all the three structures, the 2D FS show additional FAs pointing outward for Set 1 WPs (see  $k_x=0.3$  (1/Å) in Fig.5(d), (h) and (l)). These line-shaped FAs are aligned along the inner hexagon of bulk band projection around the  $\bar{\Gamma}$  point, which have not been found before in earlier studies and are the new features we predicted for the (0001) surface of  $\gamma$ -PtBi<sub>2</sub>. In our early study<sup>44</sup> of ZrTe<sub>5</sub>, it has been shown that the inward or outward FA connection can switch direction with different lattice distortions as induced by coherent phonons. Here for  $\gamma$ -PtBi<sub>2</sub>, the inversion symmetry is already broken, while the switching of the FA connection happens at different energies.

Despite the differences in the number of WP sets, the bulk gap region midway of the  $\bar{\Gamma}$ - $\bar{M}$  direction is the common theme for all the three structures. To better understand

the dispersion of the FA associated surface states, using the averaged structure, we plot in Fig.6 the surface spectral functions with cuts indicated in Fig.6(a) with the bulk only contribution in the last column. The 2D FS at  $E_F$  in Fig.6(a) and (e) for the A and B-terminations have the similar FA features to the  $\pm 0.012$  eV in Fig.3 and 4. For the first cut passing directly through a pair of Set 1 WPs, the  $W_1^-$  and  $W_1^+$  at  $E_F + 0.055$  eV can be clearly seen in Fig.6(j) as labeled near the bulk gap region with vertical lines. For the A-termination in Fig.6(b), the surface states follow the bottom rim of the bulk gap region and converge to Set 1 WP projection. On the B-termination in Fig.6(f), the surface states are instead overlayed on the bulk band projection but also converge to Set 1WP projection. Moving to the second cut on the right in Fig.6(k), the top of bulk valence band in the middle goes up in energy to  $+0.130$  eV. The surface states for B-termination in Fig.6(g) also go up in energy. Interestingly for A-termination in Fig.6(c), the surface states are still at the bottom rim of the bulk gap region, showing the robustness. With the third cut further to the right in Fig.6(l), the top of bulk valence bands in the middle are pushed up even higher in energy to  $+0.200$  eV and cross with the bulk conduction bands to have more accidental crossings as confirmed by the extra sets of WPs at  $+0.200$  eV and above. At the same time, the bottom of bulk conduction bands on the other side of the bulk gap region in Fig.6(l) drops to lower energy and almost touches the bulk valence band around the  $E_F$ , which can result in the Set 2 WPs just below the  $E_F$  as seen for the less Bi-buckling structure. For A-termination in Fig.6(d), the surface states at the bottom rim of bulk gap region remain robust. Interestingly for the B-termination in Fig.6(h), the original surface states are pushed to energy above  $0.120$  eV, but new surface states emerge at the bottom rim of the bulk gap region, giving the FAs at the far side of the bulk gap region in 2D FS of Fig.6(e).

As mentioned earlier, the FAs connection between the robust Set 1 WP can switch direction at higher energy. Also to explore the FAs for the extra sets of WPs, we have plotted 2D FS and QPI in Fig.7 at  $+0.100$  eV for the averaged structure. For the A-termination in Fig.7(a), the surface states form the FAs connecting among the extra sets of WPs as more clearly seen in the surface only contribution in Fig.7(c). For the B-termination in Fig.7(b), the FAs are the curly surface states (Fig.7(d)) stemming outward from Set 1 WPs with high intensity. Correspondingly, the QPI for A-termination in Fig.7(e) shows a different pattern from the QPI near  $E_F$  in Fig.3 and 4. The QPI for B-termination in Fig.7(f)

has more prominent patterns from the curly FAs. These calculated QPI patterns at  $E_F+0.100$  eV are from the predicted new FA features and need future experiments to investigate.

## IV. Conclusion

In conclusion, we have used first-principles calculations and Wannier functions to explore the band crossings throughout the full Brillouin zone (BZ) between the nominally highest valence and lowest conduction bands in  $\gamma$ -PtBi<sub>2</sub> with different structural parameters. We find that the main difference between the two experimentally reported structural parameters<sup>1, 12</sup> is the magnitude of the Bi-layer buckling. By calculating band structures of both more and less Bi-layer buckling structures as well as the averaged one, we find a Weyl nodal loop (WNL) and multiple sets of Weyl points (WPs). The robust features are the WNL on the  $\Gamma$ -K-A plane as protected by the mirror symmetry, the bulk gap region with the set of WPs just above the Fermi energy ( $E_F$ ) from the main band inversion along the  $\bar{\Gamma}$ - $\bar{M}$  direction. In contrast, the number and locations of other multiple sets of WPs are sensitive to the Bi-layer buckling. We study the evolution of the Fermi arcs around the bulk gap region. Besides calculating the 2D Fermi surface and quasi-particle interference (QPI) in good agreements with ARPES and experimental QPI, we predict new Fermi arc features and the related QPI pattern at  $E_F+100$  meV, which need to be verified in future experiments.

**Data Availability:** The data that support the findings of this study are openly available<sup>45</sup>.

## Acknowledgements

We acknowledge helpful discussions with Adam Kaminski, Hermann Suderow and Paul C. Canfield. This work was supported by the U.S. Department of Energy Office of Science, Office of Basic Energy Sciences through the Ames National Laboratory. The Ames National Laboratory is operated for the U.S. Department of Energy by Iowa State University under Contract No. DE-AC02-07CH11358. Some of this research used resources of the National Energy Research Scientific Computing Center (NERSC), a DOE Office of Science User Facility.

Table 1. Experimental<sup>1, 12</sup>, averaged and relaxed lattice parameters of trigonal  $\gamma$ -PtBi<sub>2</sub>. For ionic relaxation, the unit cell lattice constants are fixed to the experimental values with the internal coordinates relaxed in different exchange-correlation functionals of PBE<sup>31</sup>, D3<sup>37</sup>, optB86b<sup>38</sup> and r2SCAN+rVV10<sup>39</sup>.

	$a$ (Å)	$c$ (Å)	$x_{\text{Pt}}$	$x_{\text{Bi3}}$	$z_{\text{Bi3}}$	$z_{\text{Bi2}}$	$z_{\text{Bi1}}$	$d_{\text{Bi2-Bi1}}$ (Å)
Ref. <sup>12</sup>	6.5731	6.1619	0.2619	0.3856	0.767	0.292	0.137	0.955
Ref. <sup>1</sup>	6.573	6.1665	0.263	0.38876	0.77284	0.28429	0.15486	0.798
Avg.	6.57305	6.1642	0.26245	0.38718	0.76992	0.28814	0.14593	0.877
PBE			0.26030	0.39193	0.77795	0.28014	0.14694	0.821
D3			0.26310	0.39018	0.77897	0.27885	0.14870	0.803
optB86b			0.26067	0.39108	0.77803	0.27986	0.14730	0.817
r2SCAN+rVV10			0.26506	0.38716	0.77447	0.28081	0.15645	0.767

Table 2. Momentum-energy of different sets of Weyl point (WP) using the experimental<sup>1, 12</sup>, and averaged lattice parameters of trigonal  $\gamma$ -PtBi<sub>2</sub>. The band structures are calculated with mBJ and fitted to a tight-binding Hamiltonian with Wannier functions.

Lattice	WP set	Momentum ( $k_x, k_y, k_z$ ) (1/Å)	$E - E_F$ (eV)
Avg.	1	(0.33216, 0.03110, -0.13023)	0.055
	2	(0.43218, 0.14289, -0.27762)	0.234
	3	(0.37573, 0.13282, -0.29144)	0.279
	4	(0.40425, 0.19143, -0.37676)	0.313
	5	(0.40396, 0.14193, -0.30754)	0.325
	6	(0.39015, 0.19729, -0.35641)	0.339
Ref. <sup>12</sup>	1	(0.31898, 0.03920, -0.14161)	0.033
	2	(0.34309, 0.11210, -0.26517)	0.181
Ref. <sup>1</sup>	1	(0.34067, 0.02352, -0.11875)	0.072
	2	(0.43178, 0.01384, -0.03291)	-0.015
	3	(0.45107, 0.13725, -0.28224)	0.226
	4	(0.44785, 0.13626, -0.36634)	0.319
	5	(0.39474, 0.16978, -0.32786)	0.356

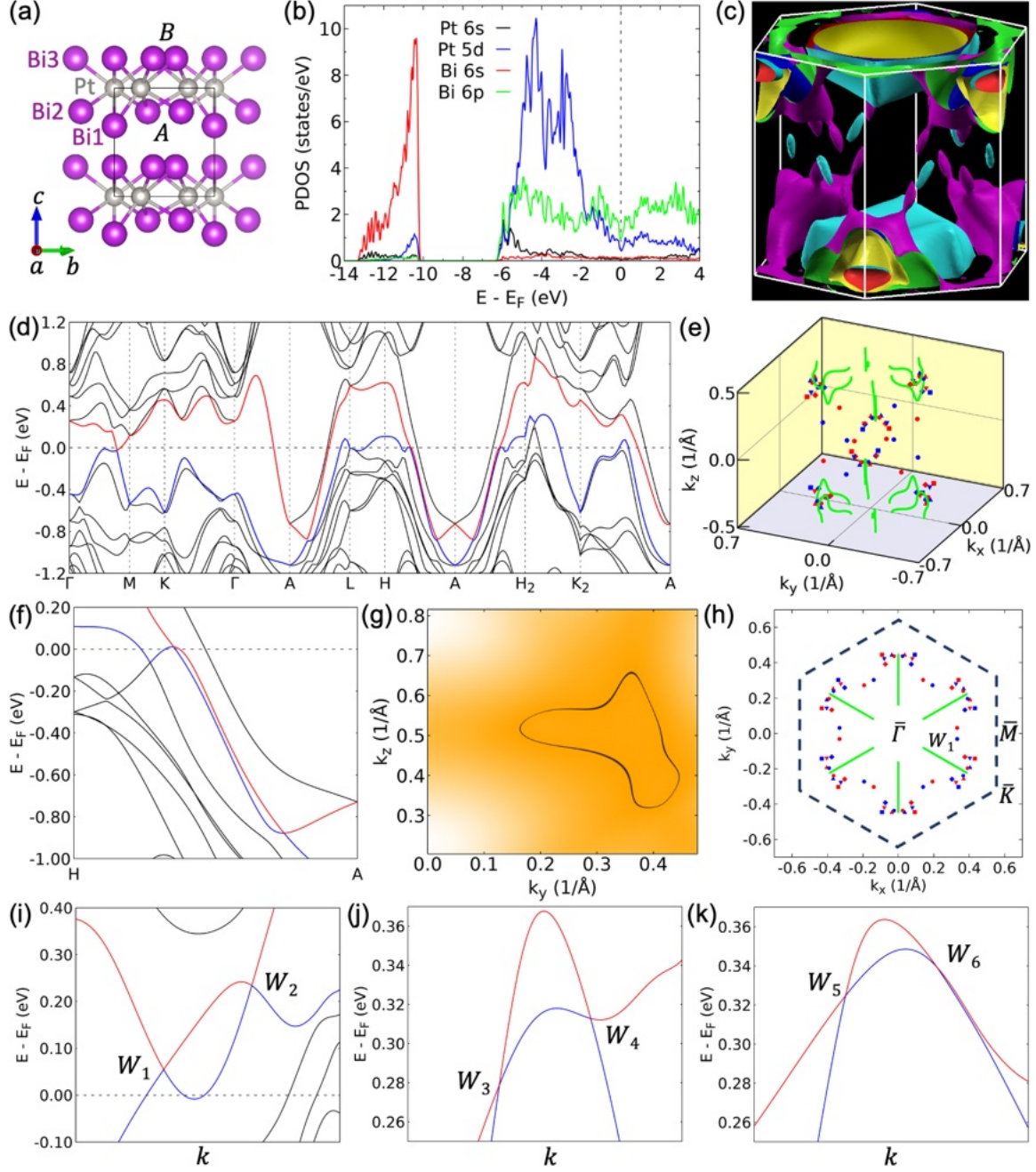


Figure 1. Band structure of  $\gamma$ -PtBi<sub>2</sub>. (a) Crystal structure with (0001) surface A- and B- terminations. (b) Projected density of states (PDOS), (c) 3D Fermi surface, (d) band structure along high-symmetry directions. The nominally highest valence and lowest conduction bands are in blue and red, respectively. (e) Six sets of Weyl points (WPs) and one set of Weyl nodal loop. (f) Band structure zoomed along the  $H$ - $A$  direction. (g) Zero-gap contour on the  $k_y$ - $k_z$  or  $M_x$  mirror plane. (h) Projection on the (0001) plane of (e) with the six sets of WPs labeled. (i-k) Band dispersion near the six set of WPs as labeled.

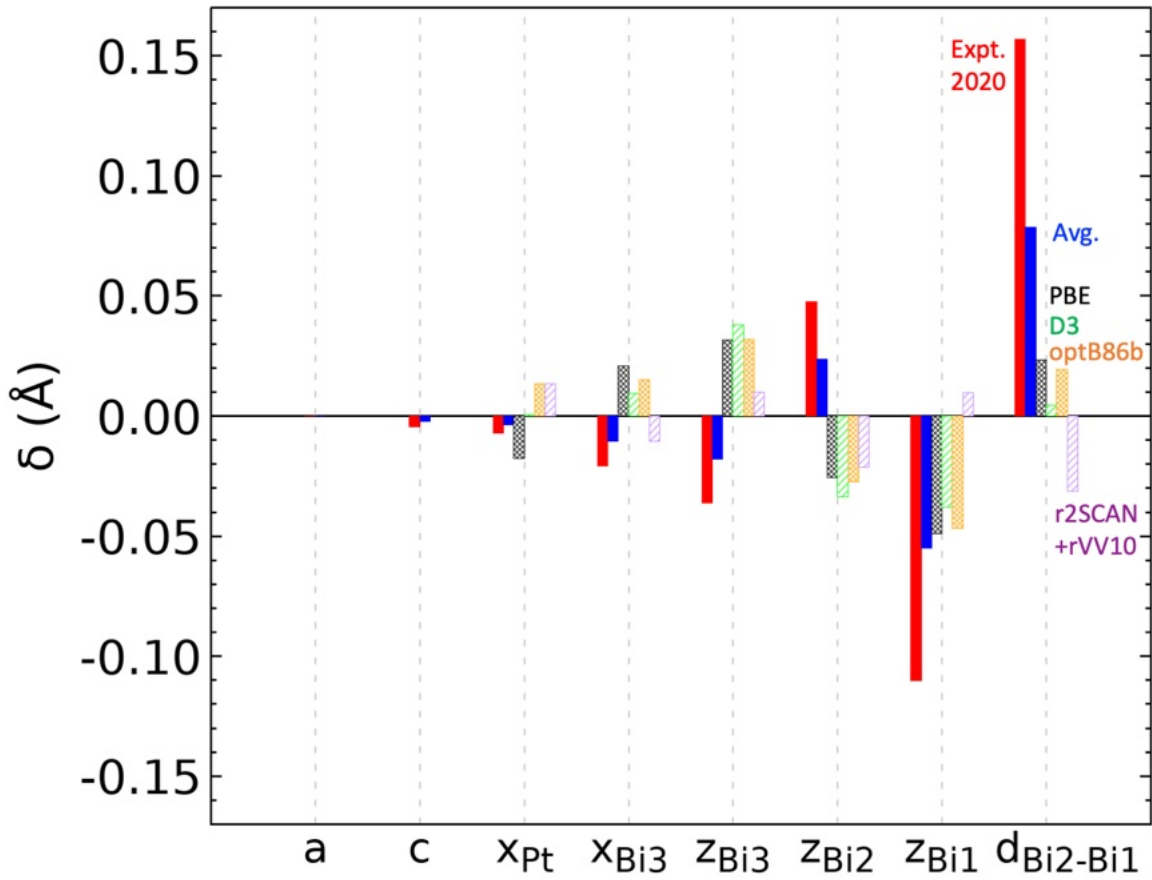


Figure 2. Difference of structural parameters of  $\gamma$ -PtBi<sub>2</sub> with respect to the experimental values in 2014 of Ref.<sup>1, 12</sup>. The corresponding data of these parameters are listed in Table 1. The ionic relaxations in DFT are with exchange-correlation functionals of PBE, D3, optB86b and r2SCAN+rVV10, respectively. The averaged (Avg.) data are between the two experimental data of Ref.<sup>1</sup> in 2014 and Ref.<sup>12</sup> in 2020.

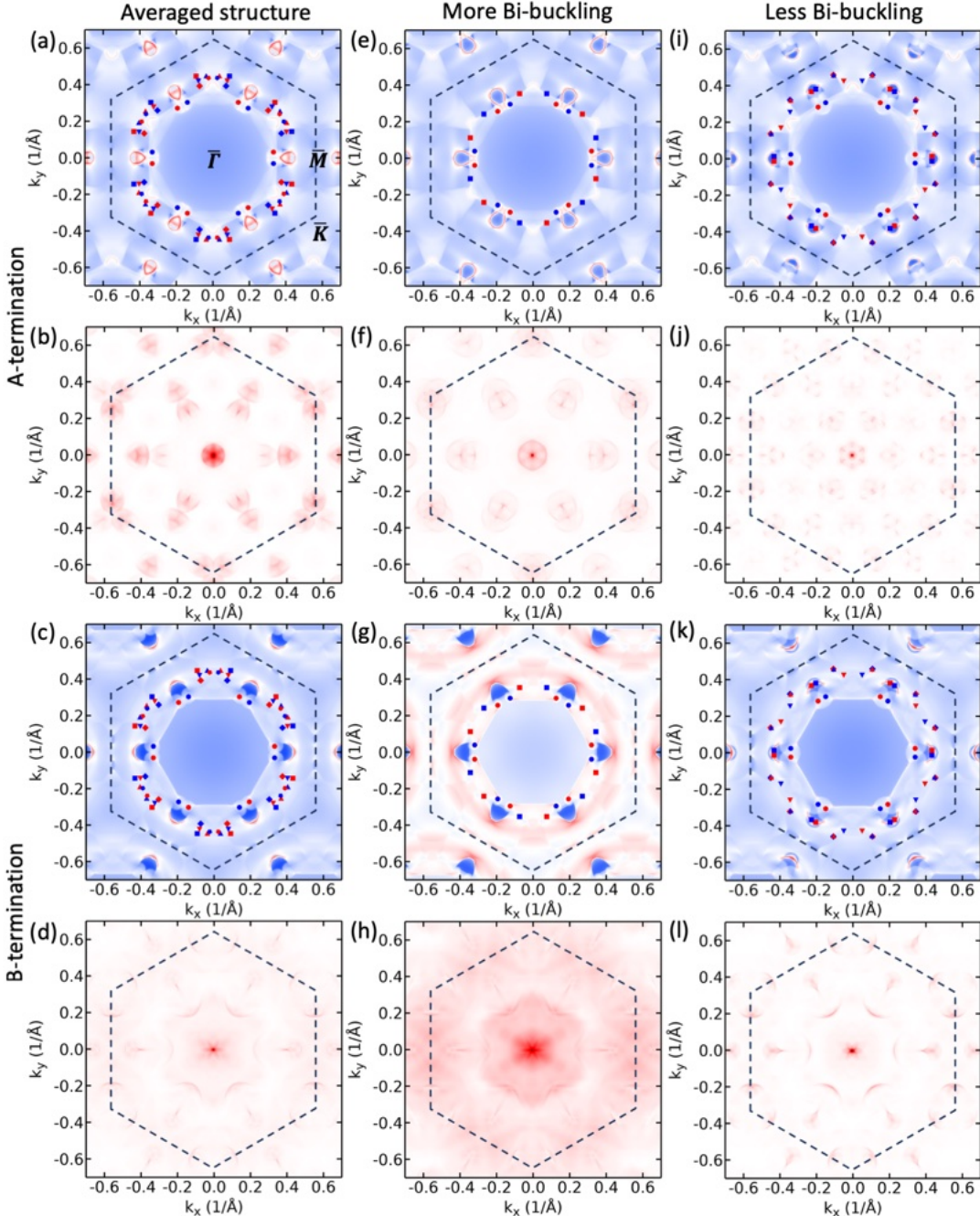


Figure 3. 2D Fermi surface and QPI of  $\gamma$ -PtBi<sub>2</sub> (0001) at  $E_F=0.012$  eV calculated with different lattice parameters. Panel (a-d) are from the averaged experimental lattice parameters of Ref.<sup>12</sup> ((e-h)) with more Bi-buckling and Ref.<sup>1</sup> ((i-l)) with less Bi-buckling. For each column, top (bottom) two rows are for A (B) termination with 2D Fermi surface showing Fermi arcs and the corresponding QPI. For Fermi surface, red (blue) stands for high (low) intensity. For QPI, red (white) stands for high (low) intensity. The associated multiple sets of Weyl points are labeled in 2D Fermi surface as different symbol shapes with red (blue) for positive (negative) chirality.

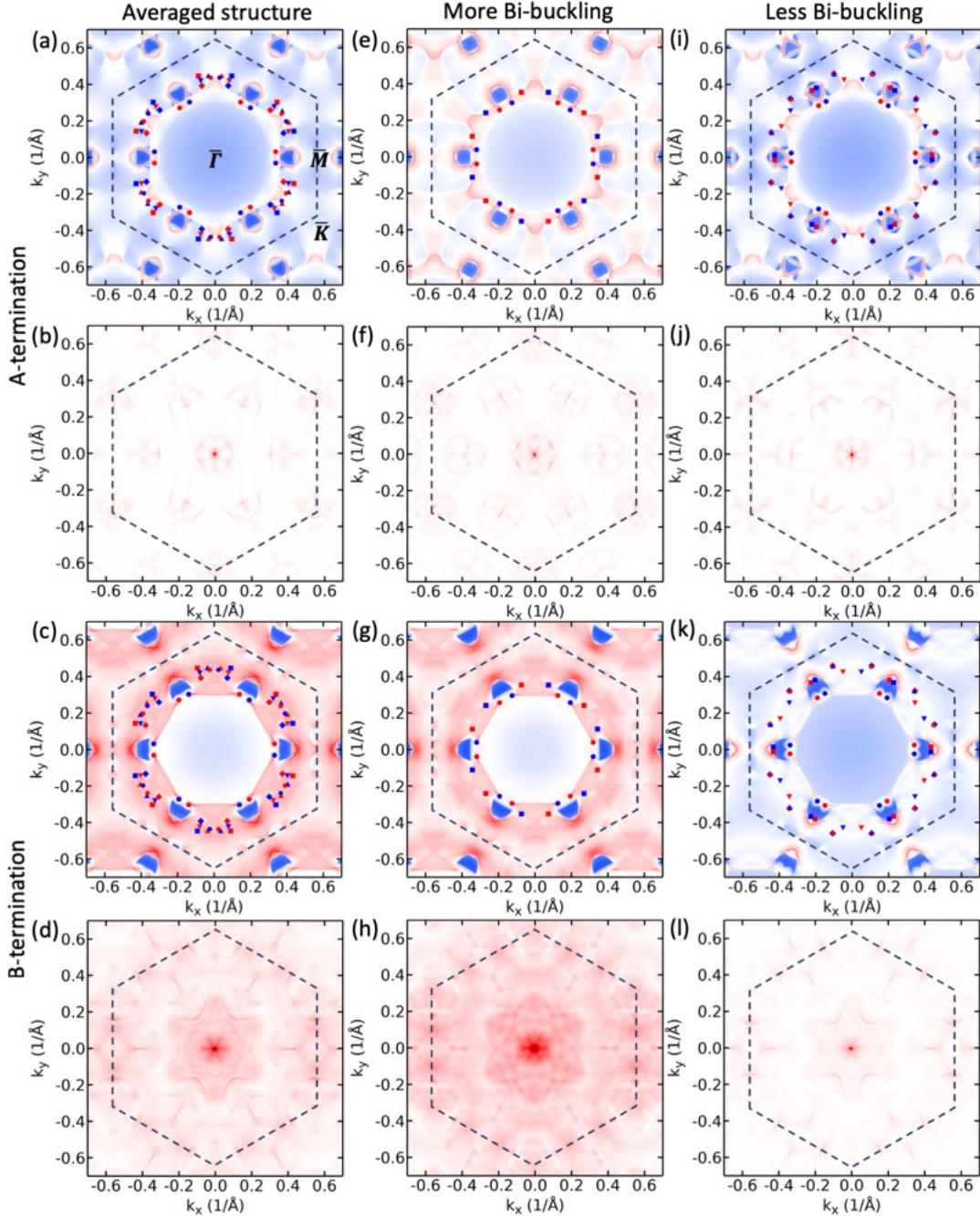


Figure 4. 2D Fermi surface and QPI of  $\gamma$ -PtBi<sub>2</sub> (0001) at  $E_F+0.012$  eV calculated with different lattice parameters. Panel (a-d) are from the averaged experimental lattice parameters of Ref.<sup>12</sup> ((e-h)) with more Bi-buckling and Ref.<sup>1</sup> ((i-l)) with less Bi-buckling. For each column, top (bottom) two rows are for A (B) termination with 2D Fermi surface showing Fermi arcs and the corresponding QPI. For Fermi surface, red (blue) stands for high (low) intensity. For QPI, red (white) stands for high (low) intensity. The associated multiple sets of Weyl points are labeled in 2D Fermi surface as different symbol shapes with red (blue) for positive (negative) chirality.

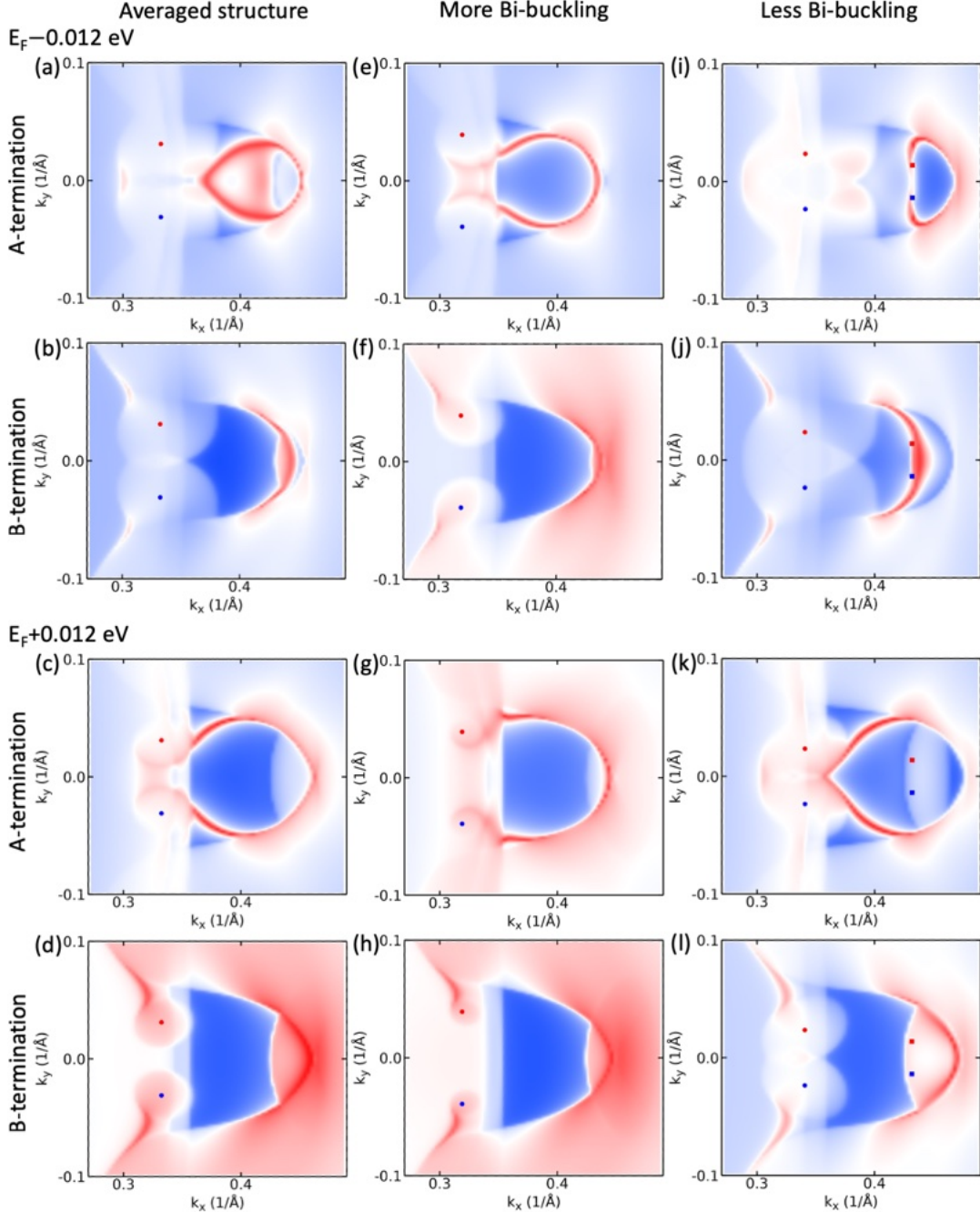


Figure 5. 2D Fermi surface of  $\gamma$ -PtBi<sub>2</sub> (0001) zoomed in around the projection of Set 1 Weyl point calculated with different structural parameters. Panel (a-d) are with the averaged experimental parameters of Ref.<sup>12</sup> ((e-h) with more Bi-buckling) and Ref.<sup>1</sup> ((i-l) with less Bi-buckling). For each column, top (bottom) two rows are for  $E_F - 0.012$  eV ( $E_F + 0.012$  eV) with A and B-terminations. For Fermi surface, red (blue) stands for high (low) intensity. For QPI, red (white) stands for high (low) intensity. The associated sets of Weyl points are labeled in 2D Fermi surface as different symbol shapes with red (blue) for positive (negative) chirality.

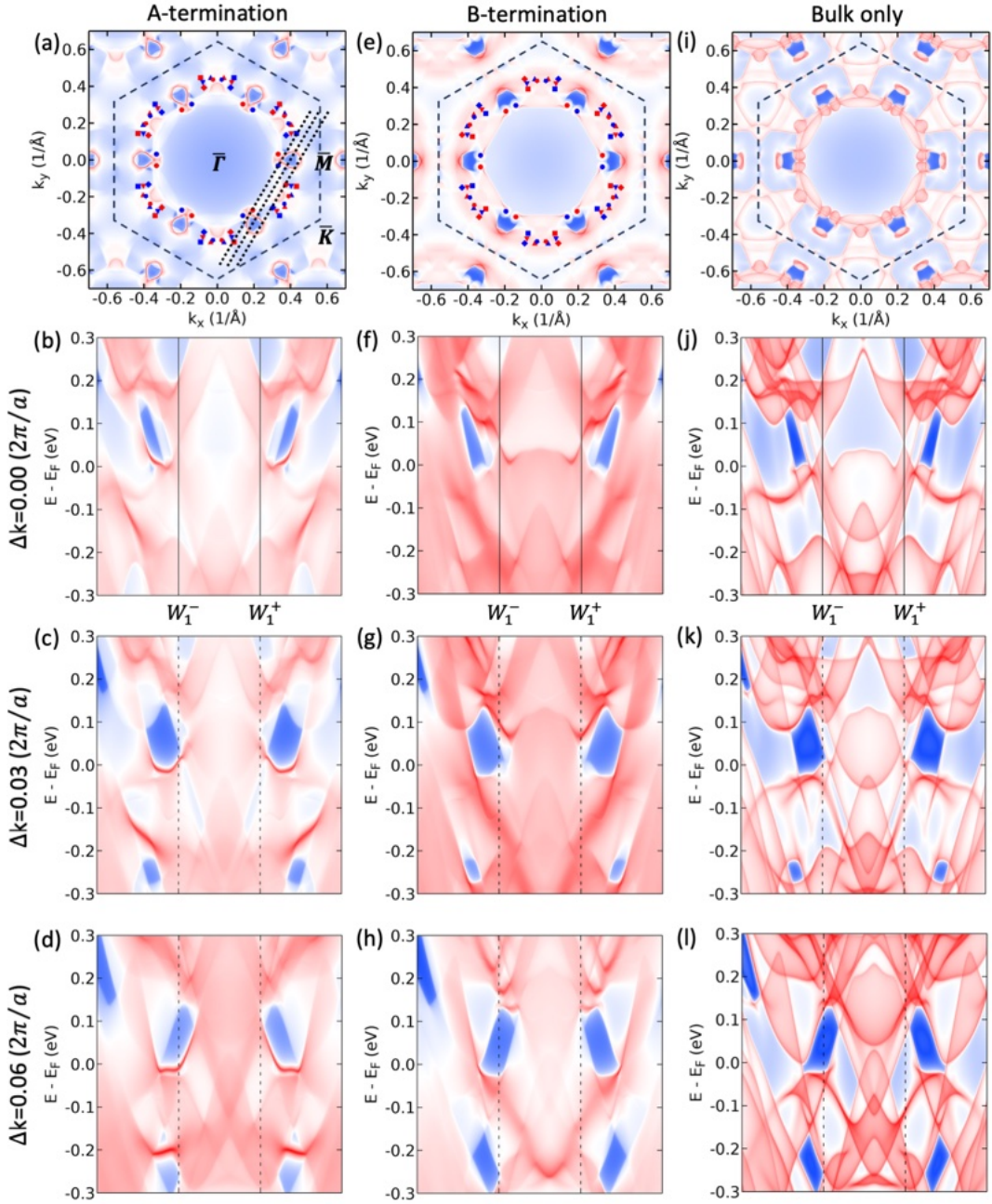


Figure 6. Surface spectral function of  $\gamma$ -PtBi<sub>2</sub> (0001) calculated with the averaged experimental lattice parameters. The columns are for A, B-termination and bulk only contributions. Panel (a-b) are the 2D Fermi surface with the multiple sets of Weyl points labeled as different symbol shapes with red (blue) for positive (negative) chirality. In (a), the first dashed line on the left is the cut across the Set 1 Weyl points (W1) with the surface spectral function shown in the rows. The two additional dashed lines are cut shifted along the b1-axis as labeled in each row. In each panel, red (blue) stands for high (low) intensity.

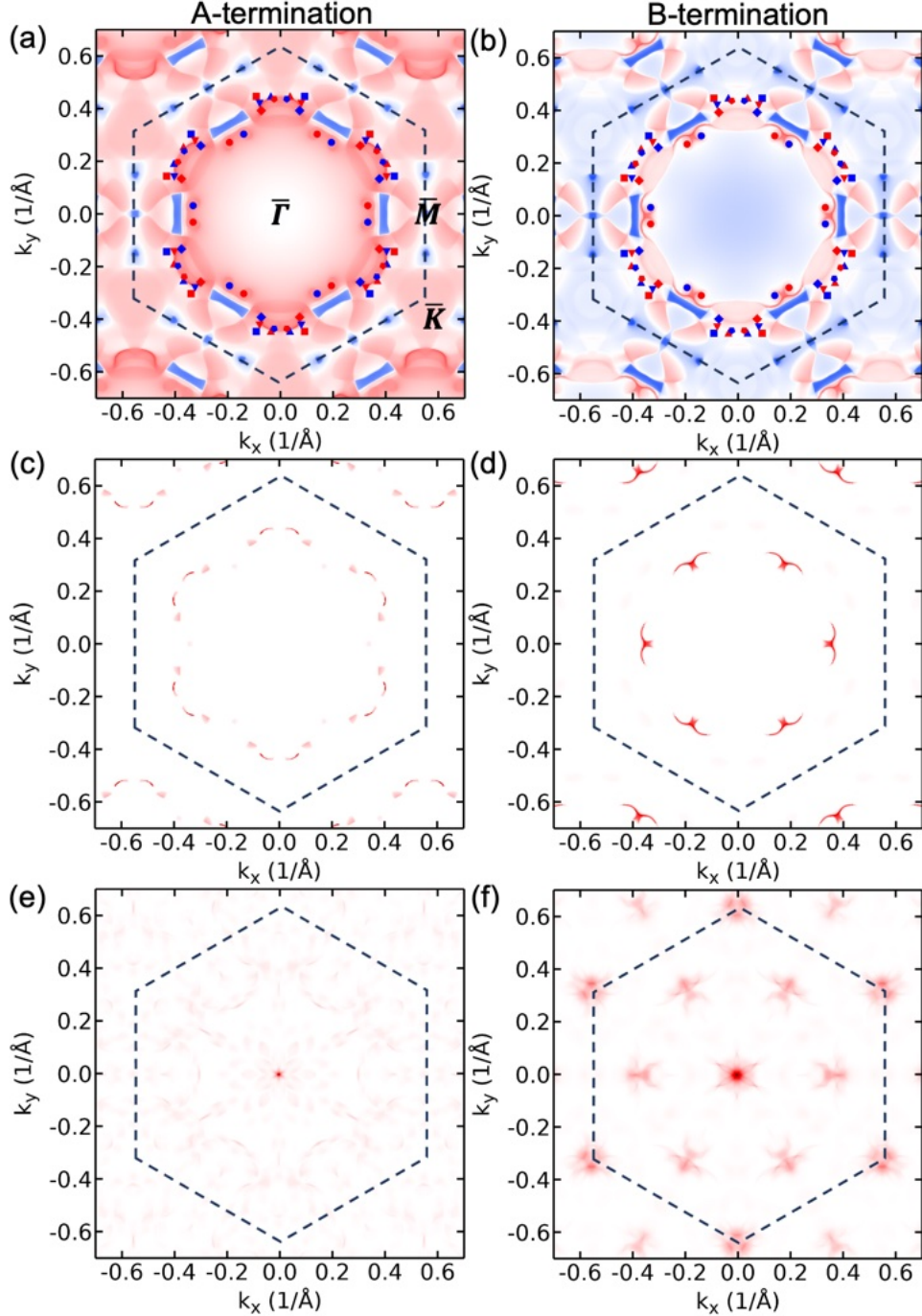


Figure 7. 2D Fermi surface and QPI of  $\gamma$ -PtBi<sub>2</sub> (0001) at  $E_F+0.100$  eV calculated with the averaged experimental lattice parameters. The two columns are for the A and B-termination, respectively. (c-d) Fermi surface with only surface state contribution and (e-f) the corresponding QPI. For Fermi surface, red (blue) stands for high (low) intensity. For surface state only contribution and QPI, red (white) stands for high (low) intensity. The multiple sets of Weyl points are labeled in 2D Fermi surface as different symbol shapes with red (blue) for positive (negative) chirality.

## References

1. M. Kaiser, A. I. Baranov, M. Ruck,  $\text{Bi}_2\text{Pt}(\text{hP9})$  by Low-Temperature Reduction of  $\text{Bi}_{13}\text{Pt}_3\text{I}_7$ : Reinvestigation of the Crystal Structure and Chemical Bonding Analysis. *Z Anorg Allg Chem* **640**, 2742-2746 (2014).
2. X. Yang, H. Bai, Z. Wang, Y. Li, Q. Chen, J. Chen, Y. Li, C. Feng, Y. Zheng, Z.-a. Xu, Giant linear magneto-resistance in nonmagnetic  $\text{PtBi}_2$ . *Appl Phys Lett* **108**, 252401 (2016).
3. W. Gao, X. Zhu, F. Zheng, M. Wu, J. Zhang, C. Xi, P. Zhang, Y. Zhang, N. Hao, W. Ning, M. Tian, A possible candidate for triply degenerate point fermions in trigonal layered  $\text{PtBi}_2$ . *Nat Commun* **9**, 3249 (2018).
4. L. Xing, R. Chapai, R. Nepal, R. Jin, Topological behavior and Zeeman splitting in trigonal  $\text{PtBi}_{2-x}$  single crystals. *Npj Quantum Mater* **5**, 10 (2020).
5. Y. Feng, Q. Jiang, B. Feng, M. Yang, T. Xu, W. Liu, X. Yang, M. Arita, E. F. Schwier, K. Shimada, H. O. Jeschke, R. Thomale, Y. Shi, X. Wu, S. Xiao, S. Qiao, S. He, Rashba-like spin splitting along three momentum directions in trigonal layered  $\text{PtBi}_2$ . *Nat Commun* **10**, 4765 (2019).
6. Q. Yao, Y. P. Du, X. J. Yang, Y. Zheng, D. F. Xu, X. H. Niu, X. P. Shen, H. F. Yang, P. Dudin, T. K. Kim, M. Hoesch, I. Vobornik, Z. A. Xu, X. G. Wan, D. L. Feng, D. W. Shen, Bulk and surface electronic structure of hexagonal structured  $\text{PtBi}_2$  studied by angle-resolved photoemission spectroscopy. *Phys Rev B* **94**, 235140 (2016).
7. S. Thirupathaiah, Y. Kushnirenko, E. Haubold, A. V. Fedorov, E. D. L. Rienks, T. K. Kim, A. N. Yaresko, C. G. F. Blum, S. Aswartham, B. Büchner, S. V. Borisenko, Possible origin of linear magnetoresistance: Observation of Dirac surface states in layered  $\text{PtBi}_2$ . *Phys Rev B* **97**, 035133 (2018).
8. X.-A. Nie, S. Li, M. Yang, Z. Zhu, H.-K. Xu, X. Yang, F. Zheng, D. Guan, S. Wang, Y.-Y. Li, C. Liu, J. Li, P. Zhang, Y. Shi, H. Zheng, J. Jia, Robust Hot Electron and Multiple Topological Insulator States in  $\text{PtBi}_2$ . *ACS Nano* **14**, 2366-2372 (2020).
9. A. Veyrat, V. Labracherie, D. L. Bashlakov, F. Caglieris, J. I. Facio, G. Shipunov, T. Charvin, R. Acharya, Y. Naidyuk, R. Giraud, J. van den Brink, B. Büchner, C. Hess, S. Aswartham, J. Dufouleur, Berezinskii–Kosterlitz–Thouless Transition in the Type-I Weyl Semimetal  $\text{PtBi}_2$ . *Nano Lett* **23**, 1229-1235 (2023).
10. A. Kuibarov, O. Suvorov, R. Vocaturo, A. Fedorov, R. Lou, L. Merkwitz, V. Voroshnin, J. I. Facio, K. Koepernik, A. Yaresko, G. Shipunov, S. Aswartham, J. v. d. Brink, B. Büchner, S. Borisenko, Evidence of superconducting Fermi arcs. *Nature* **626**, 294-299 (2024).
11. S. Schimmel, Y. Fasano, S. Hoffmann, J. Besproswanny, L. T. Corredor Bohorquez, J. Puig, B.-C. Elshalem, B. Kalisky, G. Shipunov, D. Baumann, S.

Aswartham, B. Büchner, C. Hess, Surface superconductivity in the topological Weyl semimetal t-PtBi<sub>2</sub>. *Nat Commun* **15**, 9895 (2024).

12. G. Shipunov, I. Kovalchuk, B. R. Piening, V. Labracherie, A. Veyrat, D. Wolf, A. Lubk, S. Subakti, R. Giraud, J. Dufouleur, S. Shokri, F. Caglieris, C. Hess, D. V. Efremov, B. Büchner, S. Aswartham, Polymorphic PtBi<sub>2</sub>: Growth, structure, and superconducting properties. *Physical Review Materials* **4**, 124202 (2020).
13. J. Wang, X. Chen, Y. Zhou, C. An, Y. Zhou, C. Gu, M. Tian, Z. Yang, Pressure-induced superconductivity in trigonal layered PtBi<sub>2</sub> with triply degenerate point fermions. *Phys Rev B* **103**, 014507 (2021).
14. D. L. Bashlakov, O. E. Kvintitskaya, G. Shipunov, S. Aswartham, O. D. Feya, D. V. Efremov, B. Büchner, Y. G. Naidyuk, Electron-phonon interaction and point contact enhanced superconductivity in trigonal PtBi<sub>2</sub>. *Low Temperature Physics* **48**, 747-754 (2022).
15. R. Vocaturo, K. Koepernik, J. I. Facio, C. Timm, I. C. Fulga, O. Janson, J. van den Brink, Electronic structure of the surface-superconducting Weyl semimetal PtBi<sub>2</sub>. *Phys Rev B* **110**, 054504 (2024).
16. E. O'Leary, Z. Li, L.-L. Wang, B. Schrunk, A. Eaton, P. C. Canfield, A. Kaminski, Topography of Fermi arcs in t-PtBi<sub>2</sub> using high-resolution angle-resolved photoemission spectroscopy. *Phys Rev B* **112**, 085154 (2025).
17. S. Hoffmann, S. Schimmel, R. Vocaturo, J. Puig, G. Shipunov, O. Janson, S. Aswartham, D. Baumann, B. Büchner, J. v. d. Brink, Y. Fasano, J. I. Facio, C. Hess, Fermi Arcs Dominating the Electronic Surface Properties of Trigonal PtBi<sub>2</sub>. *Advanced Physics Research* **4**, 2400150 (2025).
18. A. Kuibarov, S. Changdar, A. Fedorov, R. Lou, O. Suvorov, V. Misheneva, L. Harnagea, I. Kovalchuk, S. Wurmehl, B. Büchner, S. Borisenko, Measuring superconducting arcs by angle-resolved photoemission spectroscopy. *Phys Rev B* **112**, 144518 (2025).
19. K. Mæland, M. Bahari, B. Trauzettel, Phonon-mediated intrinsic topological superconductivity in Fermi arcs. *Phys Rev B* **112**, 104507 (2025).
20. J. A. Moreno, P. García Talavera, E. Herrera, S. López Valle, Z. Li, L.-L. Wang, S. Bud'ko, A. I. Buzdin, I. Guillamón, P. C. Canfield, H. Suderow, Robust surface superconductivity and vortex lattice in the Weyl semimetal  $\gamma$ -PtBi<sub>2</sub>. *arXiv e-prints*, arXiv:2508.04867 (2025).
21. J. Besproswanny, S. Schimmel, Y. Fasano, G. Shipunov, S. Aswartham, D. Baumann, B. Büchner, C. Hess, Temperature dependence of surface superconductivity in t-PtBi<sub>2</sub>. *arXiv e-prints*, arXiv:2507.10187 (2025).
22. X. Huang, L. Zhao, S. Schimmel, J. Besproswanny, P. Härtl, C. Hess, B. Büchner, M. Bode, Sizable superconducting gap and anisotropic chiral topological superconductivity in the Weyl semimetal PtBi<sub>2</sub>. *arXiv e-prints*, arXiv:2507.13843 (2025).

23. O. E. Kvintitskaya, L. Harnagea, G. Shipunov, S. Aswartham, V. V. Fisun, D. V. Efremov, B. Büchner, Y. G. Naidyuk, Point-contact enhanced superconductivity in trigonal  $\text{PtBi}_2$ : quest for the origin of high-Tc. *arXiv e-prints*, arXiv:2511.00920 (2025).

24. A. Nomani, P. Hosur, Intrinsic surface superconducting instability in type-I Weyl semimetals. *Phys Rev B* **108**, 165144 (2023).

25. X. Bai, W. LiMing, T. Zhou, Superconductivity in Weyl semimetals with time reversal symmetry. *New J Phys* **27**, 013003 (2025).

26. P. Hohenberg, W. Kohn, Inhomogeneous Electron Gas. *Phys. Rev.* **136**, B864-B871 (1964).

27. W. Kohn, L. J. Sham, Self-Consistent Equations Including Exchange and Correlation Effects. *Phys. Rev.* **140**, A1133-A1138 (1965).

28. N. Marzari, D. Vanderbilt, Maximally localized generalized Wannier functions for composite energy bands. *Phys Rev B* **56**, 12847-12865 (1997).

29. I. Souza, N. Marzari, D. Vanderbilt, Maximally localized Wannier functions for entangled energy bands. *Phys Rev B* **65**, 035109 (2001).

30. N. Marzari, A. A. Mostofi, J. R. Yates, I. Souza, D. Vanderbilt, Maximally localized Wannier functions: Theory and applications. *Rev Mod Phys* **84**, 1419-1475 (2012).

31. J. P. Perdew, K. Burke, M. Ernzerhof, Generalized gradient approximation made simple. *Phys Rev Lett* **77**, 3865-3868 (1996).

32. A. D. Becke, E. R. Johnson, A simple effective potential for exchange. *The Journal of Chemical Physics* **124**, 221101 (2006).

33. P. E. Blöchl, Projector Augmented-Wave Method. *Phys Rev B* **50**, 17953-17979 (1994).

34. G. Kresse, J. Furthmuller, Efficient Iterative Schemes for Ab initio Total-Energy Calculations Using a Plane-Wave Basis Set. *Phys Rev B* **54**, 11169-11186 (1996).

35. G. Kresse, J. Furthmuller, Efficiency of Ab-initio Total Energy Calculations for Metals and Semiconductors Using a Plane-Wave Basis Set. *Comp Mater Sci* **6**, 15-50 (1996).

36. H. J. Monkhorst, J. D. Pack, Special Points for Brillouin-Zone Integrations. *Phys Rev B* **13**, 5188-5192 (1976).

37. S. Grimme, J. Antony, S. Ehrlich, H. Krieg, A consistent and accurate ab initio parametrization of density functional dispersion correction (DFT-D) for the 94 elements H-Pu. *The Journal of Chemical Physics* **132**, 154104 (2010).

38. J. Klimes, D. R. Bowler, A. Michaelides, Van der Waals density functionals applied to solids. *Phys Rev B* **83**, 195131 (2011).

39. J. Ning, M. Kothakonda, J. W. Furness, A. D. Kaplan, S. Ehlert, J. G. Brandenburg, J. P. Perdew, J. Sun, Workhorse minimally empirical dispersion-

corrected density functional with tests for weakly bound systems: r2SCAN+rVV10. *Phys Rev B* **106**, 075422 (2022).

- 40. H. Inoue, A. Gyenis, Z. Wang, J. Li, S. W. Oh, S. Jiang, N. Ni, B. A. Bernevig, A. Yazdani, Quasiparticle interference of the Fermi arcs and surface-bulk connectivity of a Weyl semimetal. *Science* **351**, 1184-1187 (2016).
- 41. M. P. L. Sancho, J. M. L. Sancho, J. Rubio, Quick Iterative Scheme for the Calculation of Transfer-Matrices - Application to Mo(100). *J Phys F Met Phys* **14**, 1205-1215 (1984).
- 42. M. P. L. Sancho, J. M. L. Sancho, J. Rubio, Highly Convergent Schemes for the Calculation of Bulk and Surface Green-Functions. *J Phys F Met Phys* **15**, 851-858 (1985).
- 43. Q. Wu, S. Zhang, H.-F. Song, M. Troyer, A. A. Soluyanov, WannierTools: An open-source software package for novel topological materials. *Computer Physics Communications* **224**, 405-416 (2018).
- 44. L.-L. Wang, Expansive open Fermi arcs and connectivity changes induced by infrared phonons in ZrTe<sub>5</sub>. *Phys Rev B* **103**, 075105 (2021).
- 45. L.-L. Wang, A First-principles Study of Weyl Nodal Loop and Multiple Sets of Weyl Points in Trigonal PtBi<sub>2</sub>, *Harvard Dataverse*, DRAFT VERSION (2026) doi:10.7910/DVN/EWA2OA